Lawrence Berkeley National Laboratory

Title
Evaluation of radioactive background rejection in 76Ge neutrino-less double-beta decay experiments using a highly segmented HPGe detector

Permalink

Author
Campbell, D.B.

Publication Date
2008-07-24

Peer reviewed

Evaluation of radioactive background rejection in ^{76}Ge neutrino-less double-beta decay experiments using a highly segmented HPGe detector

D.B. Campbell [a],* K. Vetter [a] R. Henning [b] K. Lesko [b]
Y.D. Chan [b] A.W.P. Poon [b] M. Perry [b,c] D. Hurley [b]
A.R. Smith [b]

[a]*Lawrence Livermore National Laboratory, Livermore, CA 94551, USA*
[b]*Lawrence Berkeley National Laboratory, Berkeley, CA 94720, USA*
[c]*Florida State University, Tallahassee, FL 32306, USA*

Abstract

A highly segmented coaxial HPGe detector was operated in a low background counting facility for over 1 year to experimentally evaluate possible segmentation strategies for the proposed Majorana neutrino-less double-beta decay experiment. Segmentation schemes were evaluated on their ability to reject multi-segment events while retaining single-segment events. To quantify a segmentation scheme's acceptance efficiency the percentage of peak area due to single segment events was calculated for peaks located in the energy region 911-2614 keV. Single interaction site events were represented by the double-escape peak from the 2614 keV decay in ^{208}Tl located at 1592 keV. In spite of its prototypical nature, the detector performed well under realistic operating conditions and required only minimal human interaction. Though the energy resolution for events with interactions in multiple segments was impacted by inter-segment cross-talk, the implementation of a cross-talk correlation matrix restored acceptable resolution. Additionally, simulations utilizing the MaGe simulation package were performed and found to be in good agreement with experimental observations verifying the external nature of the background radiation.

Key words: ^{76}Ge, Segmentation, Neutrino-less double-beta decay, Ge detector
PACS: code, code

---

* Corresponding Author. Tel.: +1 925 422 5271 fax: +1 925 424 3101
  Email address: campbell61@llnl.gov (D.B. Campbell).

1 Introduction

The recent verification of neutrino oscillations (1-8) has highlighted the need to probe the nature and absolute mass scale of the neutrino. The observation of neutrino-less double-beta decay is the only practical method for characterizing the Majorana nature of the neutrino and, if observed, the half-life of the decay potentially probes the absolute mass scale of the neutrino. The Majorana collaboration (9) advocates the use of ^{76}Ge as a means for detecting neutrino-less double-beta decay. This strategy employs germanium as both source and detector, thus enhancing detection efficiency and reducing background. A region of interest $\sim$4 keV wide centered at the expected Q-value of 2039 keV will be monitored for a period of several years with tens of kilograms, possibly up to hundreds of kilograms, of HPGe enriched to 86% ^{76}Ge. Over this period, a significant number of events due to background will be observed in this energy window, possibly obfuscating any signal due to neutrino-less double-beta decay. As a result, proper background subtraction is essential. Several measures, including detector segmentation, are proposed to reject background counts observed in the region of interest.

The net distance traveled in germanium by electrons from neutrino-less double-beta decay would be on the order of 0.5 mm from the site of the decay. As a result, a neutrino-less double-beta decay which occurred in a germanium crystal would essentially be an event with a single interaction site. On the other hand, gamma rays with a similar energy are more likely to interact with the germanium crystal several times at sites separated by $\sim$1cm as energy is dissipated through Compton scattering. Hence, significant background reduction can be achieved by rejecting events which occur at multiple interaction sites. This work utilized a highly segmented HPGe detector operated under realistic conditions to experimentally evaluate possible detector segmentation schemes. The high degree of segmentation, 8 azimuthal (ϕ) segments by 5 longitudinal (z) segments, allowed different segmentation schemes to be mimicked through the combination of individual segments during analysis.

The 1592 keV double-escape peak from the 2614 keV γ-ray in ^{208}Tl decay has been successfully employed as a metric for determining the efficiency of single-site event filtering techniques (10). Double-escape events, similar to neutrino-less double-beta decays, are currently resolvable as single site events in germanium. Individual segmentation schemes were evaluated based on their ability to retain double-escape events while suppressing background events that predominately deposit energy in multiple segments.

2 Experimental Details

The detector utilized in this work was originally designed to demonstrate Compton imaging with a single highly segmented germanium crystal (11). The coaxial n-type crystal was manufactured by ORTEC and measured 5 cm in diameter and 8 cm in length with impurities reported as $5\text{x}10^{-9}$ cm^{-3} at the front of the crystal to $10\text{x}10^{-9}$ cm^{-3} at the back. The segmentation pattern was selected to optimize the system's ability to perform $360°$ imaging in a horizontal plane. The outer boron contact contained 8 azimuthal segments (each $45°$) and 5 longitudinal segments (each 1 cm in length.) These segments were isolated from the front and rear of the crystal, by 2 cm and 1 cm respectively, to distance them from non-uniform electric fields. The inner lithium contact was not segmented. Compact preamplifiers were mounted on a circular motherboard next to the cryostat. The preamplifiers and a schematic of the segmentation pattern are shown in Figure 1. A digital signal acquisition system built by Struck Innovative Systems digitized the 42 detector channels (40 segments plus the front cap and the central contact) at a sampling rate of 100 MHz and a vertical resolution of 12 bits. The data were read through a VME-PCI interface and recorded on an acquisition computer.

The detector monitored ambient radiation at Lawrence Berkeley National Laboratory's low background counting facility in the powerplant of the Oroville dam located in Oroville, California. The facility is 180 m underground with a rating of 480 mwe (12). Additional shielding was provided by a 2 inch thick lead castle and a 0.5 inch thick inner shield of electroformed copper. The detector operated continuously for 14 months with only a single elective power cycling. Human interactions with the system were limited to filling the liquid nitrogen dewar and replacing hard disk drives used for data storage. Over 2 TB of data were recorded, including the traces from each segment for every event. The average event rate was less than 1 Hz with a 5 keV trigger threshold. A significantly lower event rate would have been observed with a detector designed for low background work and shielding fabricated from appropriately selected material. Additional, increasing the triggering threshold would have further reduced the event rate. Individual segment energy resolution was on the order of 2.4 keV at 1460 keV. This reduction in resolution from the previously reported 1.9 keV at 1332 keV (11) was most likely due to the increased vibration and noise from the six turbine generators operating at the powerplant. Individual segment energy calibrations were determined from prominent background peaks, primarily due to decays in the ^{232}Th chain. Calibrations remained stable for the course of the experiment with the exception of a single shift, on the order of 2.5 keV, due to the power cycling of the system. The data discussed here constituted measurements taken during a live time of $\sim$19,322,000s, or $\sim$224 days.

3 Results

Data analysis was hampered by the presence of cross-talk primarily between longitudinally related segments. This phenomenon occurred when the collection of charge in one segment altered the baseline of an adjacent segment due to coupling of the readout channels. Subsequently, legitimate energy deposited in an affected segment was reported inaccurately. The magnitude of the cross-talk, $\sim$1-3% of the energy deposited in the initial segment, deminished the resolution of multi-segment events to 11 keV at 1460 keV. In addition, the central contact exhibited significant degradation in energy resolution due to leakage current across the rear face of the crystal. As a result, event energy could not be determined accurately using the central contact signal.

To quantify the degree of cross-talk for each segment, events consisting of a single triggered segment were examined and the baseline deflections in the remaining segments were determined. A cross-talk correlation matrix was then constructed detailing the degree of each individual segment's effect on all other remaining segments. This allowed events susceptible to cross-talk to be identified as events containing correlated segments. The appropriate amount of energy could then be added to the cross-talk affected segments resulting in a more accurate sum energy for the event. The correction improved the energy resolution of multi-segment events to 5 keV at 1460 keV, sufficient to evaluate the merits of additional segmentation schemes. Samples of the corrected spectra are shown in Figure 2. The red spectrum contains only events with a single triggered segment according to the detector's native 8ϕ by 5z segmentation pattern. The blue spectrum contains the remaining multi-segment events. The double-escape peak is clearly present in the single segment spectrum and is missing from the multi-segment spectrum. The increased width of the ^{228}Ac 1588 keV peak, shown in the inset, is due to its predominantly multi-site nature and its subsequent susceptibility to cross-talk. The reduced magnitude of the 1588 keV peak relative to previous work (10) was consistent with the diminished level of activity of ^{228}Ac at the site. The correction of the cross-talk phenomenon allowed the multiplicity and energy of multi-segment events to be determined through the summation of individual segment energies.

4 Segmentation Analysis

The evaluated segmentation schemes were created by combining native detector segments during analysis. For example, a scheme containing only longitudinal segments, 1ϕ by 5z, was mimicked by treating each longitudinal segment's 8ϕ segments as one continuous segment. Two spectra were created for each evaluated segmentation scheme to gauge its ability to reject multi-segment

4

events while retaining single-segment events. The first spectrum contained all events from the relevant segments regardless of the number of interaction sites. The second spectrum contained the subset of those events which occurred in a single segment as determined by the scheme under examination. A series of photopeaks spanning the desired energy region, 911 to 2614 keV, were selected, including the 1592 keV double-escape peak. The area under each peak was determined in both the complete and single-segment spectra using a least-squares fitting routine which determined peak area above background. The acceptance efficiency, defined as the ratio of these peak areas $\frac{Area(M_1 Events)}{Area(M_{All} Events)}$ where M stands for multiplicity, was determined for each peak under each segmentation scheme. A sample plot for schemes differing in azimuthal segmentation, all with five longitudinal segments, is shown in Figure 3.

Due to its single-site nature, the double-escape peak at 1592 keV exhibited a consistently high acceptance efficiency ratio, retaining upward of 80% of its constituent events after a single segment cut on the data for each examined segmentation scheme. The other peaks, predominately due to higher multiplicity interactions, showed diminished acceptance efficiency which continued to decrease with increasing energy. Acceptance efficiencies for each segmentation scheme were also calculated for the continuum at the anticipated decay location of 2039 keV. These values showed roughly 50% of the background events in this region remained after a single segment cut on the data. The acceptance efficiencies for the measured peaks under each segmentaion scheme are shown in Table 1 and Table 2. The acceptance efficiencies for each of the twenty segmentation schemes are plotted in Figure 4 where each panel contains variations in the number of longitudinal segments for a given number of azimuthal segments. The examined segmentation schemes have been ranked according to acceptance efficiency of the 1460 keV peak in Figure 5. Values for the continuum and double-escape peak are shown for each segmentation scheme as well.

5 Simulations

Monte Carlo simulations were performed using MaGe (13), a simulation environment designed for the Majorana collaboration. MaGe is based on the Geant 4 (14) analysis toolkit and ROOT (15) data analysis framework. The simulation model included an 8ϕ by $5z$ segmented detector and its cryostat as well as a lead castle and copper shielding consistent with the experimental conditions. The decay of ^{40}K and the decay chain for ^{232}Th, starting at ^{228}Ra, were included in the simulation. The abbreviation of the ^{232}Th series was due to floating point precision errors in Geant 4 when dealing with nuclei with long, $\sim 10^{10}$ yr, half-lives. The subsequent effect on this analysis was negligible. The

initial decay vertices were sampled uniformly from the empty space between the inner copper shield and the cryostat. Simulated spectra were generated for each segmentation scheme and peak areas were determined with the method described above. Calculated acceptance efficiencies are shown in Table 3. A comparison between observed and simulated values for the 8ϕ by 5z segmentation pattern is shown in Figure 6. The simulations show good agreement with the data supporting the attribution of the background radiation to external sources.

6 Discussion

A highly segmented HPGe detector was placed in a low background environment and operated successfully for over one year. A minimum of effort was required to operate the detector and individual segment calibrations remained stable. Increased noise and vibration of the environment and inter-segment cross-talk, due to poorly shielded preamplifiers, adversely impacted the energy resolution of the detector. Additionally, the resolution of the central contact was degraded due to its sensitivity to leakage current. Although acceptable energy resolution was restored with a cross-talk correlation matrix, these factors should be considered when planning future experiments. Twenty possible segmentation patterns were evaluated on their ability to retain events consisting of a single segment while rejecting events composed of multiple triggered segments. Acceptance efficiencies produced using the Majorana MaGe simulation environment showed good agreement with their experimentally determined counterparts.

7 Acknowledgments

References

[1] Y. Fukuda, et al., Phys. Rev. Lett. 81 (8) (1998) 1562.

[2] Q. R. Ahmad, et al., Phys. Rev. Lett. 87 (2001) 071301.

[3]   Q. R. Ahmad, et al., Phys. Rev. Lett. 89 (2002) 011301.
[4]   K. Eguchi, et al., Phys. Rev. Lett. 90 (2003) 021802.
[5]   S. N. Ahmad, et al., Phys. Rev. Lett. 92 (2004) 181301.
[6]   Y. Ashie, et al., Phys. Rev. D 71 (2005) 112005.
[7]   B. Aharmim, et al., Phys Rev. C 72 (2005) 055502.
[8]   T. Araki, et al., Phys. Rev. Lett. 87 (2005) 081801.
[9]   C. E. Aalseth, et al., Phys. Atomic Nucl. 67 (11) (2004) 2002.
[10] S. R. Elliott, et al., Nuc. Instr. and Meth. A 558 (2006) 504.
[11] T. Niedermayr, et al., Nuc. Instr. and Meth. A 553 (2005) 501.
[12] A.R. Smith et al., Proc. SPIE 4669, (2002) 172.
[13] R. Henning et al., Nuc. Phys. B Proc. Suppl. 143, (2005) 544.
[14] S. Agnostinelli et al., Nuc. Instr. and Meth. A 506 (2003) 250.
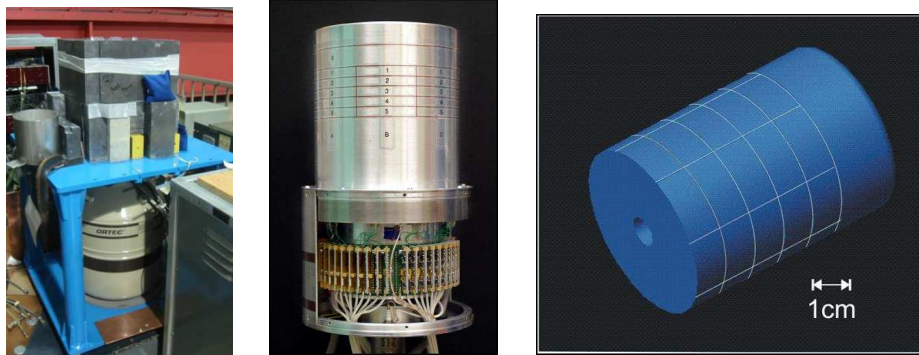[15] R. Brun et al., Nuc. Instr. and Meth. A 389 (1997) 81.

Fig. 1. Left: The detector installed at the low background counting facility. Middle: The circular motherboard containing preamplifiers. Right: A schematic illustrating the segmentation scheme of the detector.
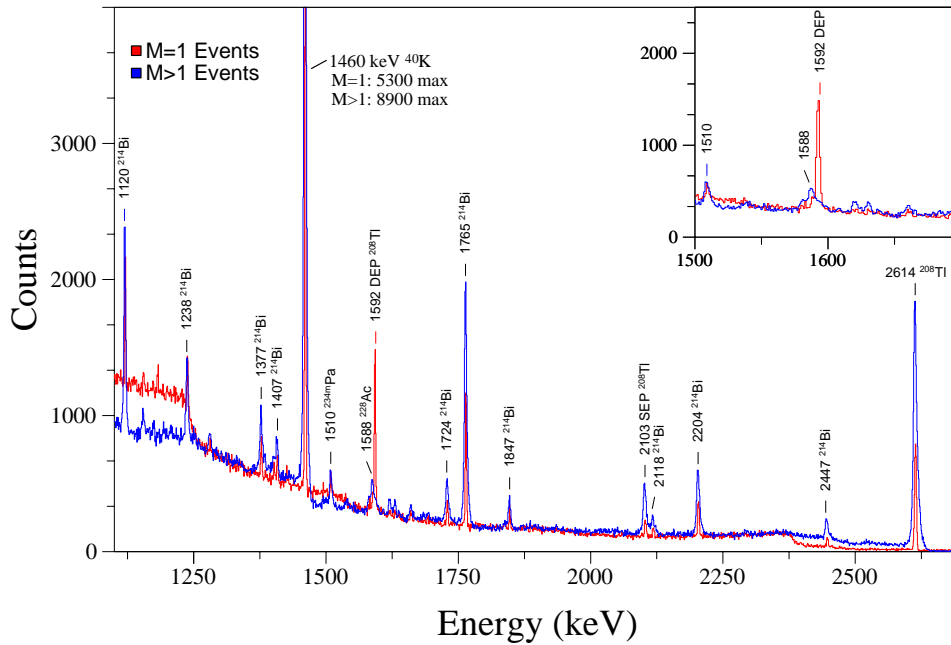

Fig. 2. Spectra depicting the data segregated according to the segmentation scheme 8ϕ by 5z. The red spectrum contains single-segment events while the blue spectrum contains events which triggered more than one segment. The inset contains an expanded view of the double-escape peak at 1592 keV and illustrates the effect of cross-talk on the 1588 keV peak.
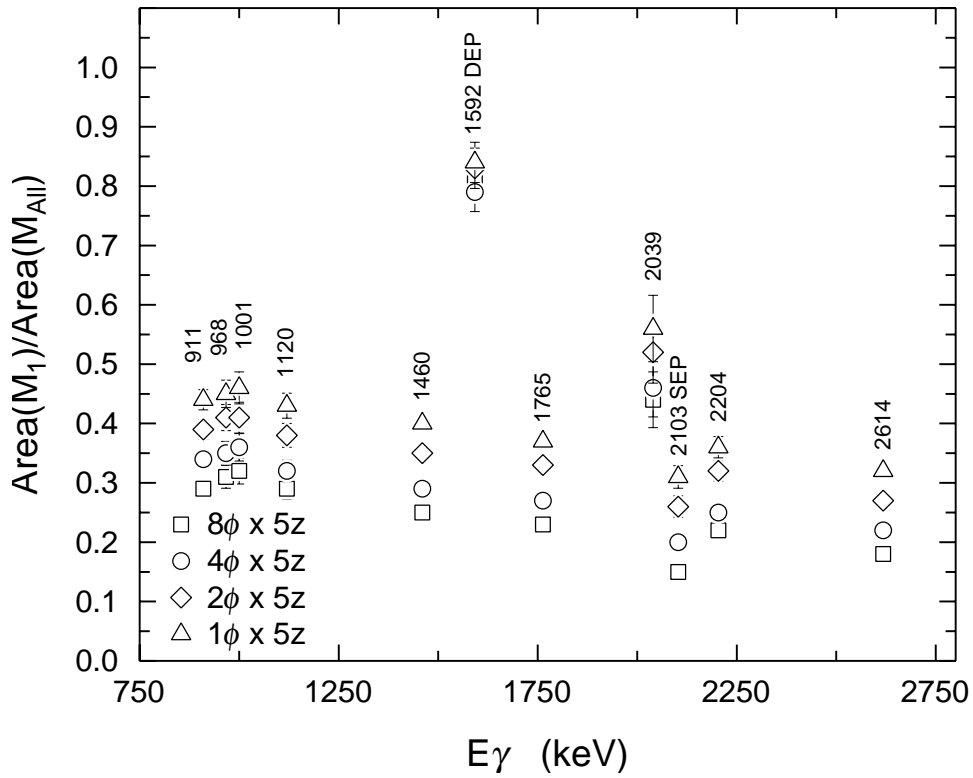
Fig. 3. A plot of acceptance efficiency ratios for different degrees of azimuthal segmentation, each scheme contains 5 longitudinal segments.

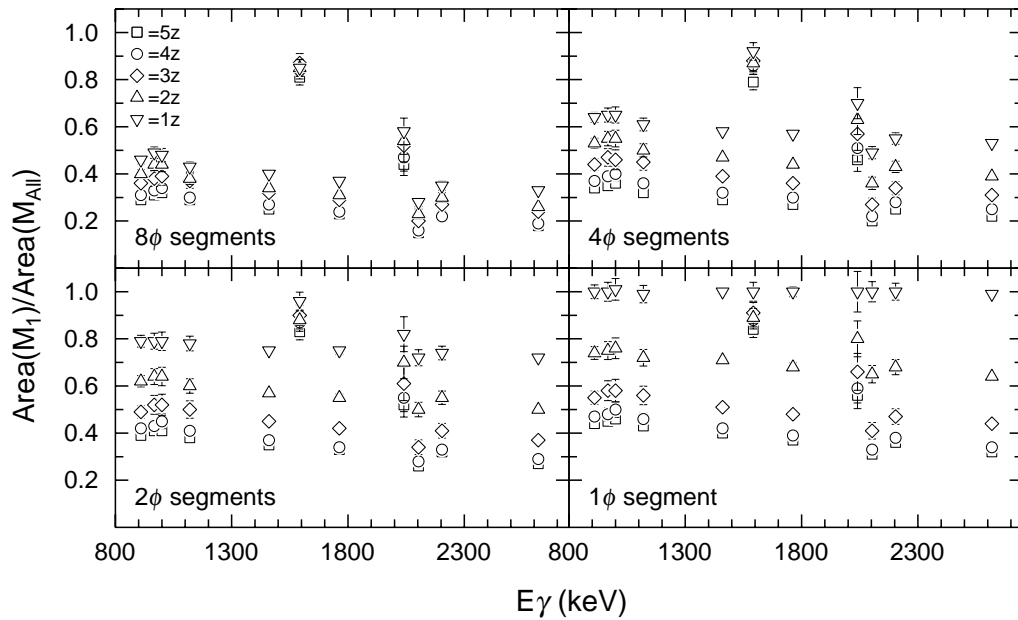Fig. 4. The measured acceptance efficiencies for each examined segmentation scheme grouped according to azimuthal segmentation.
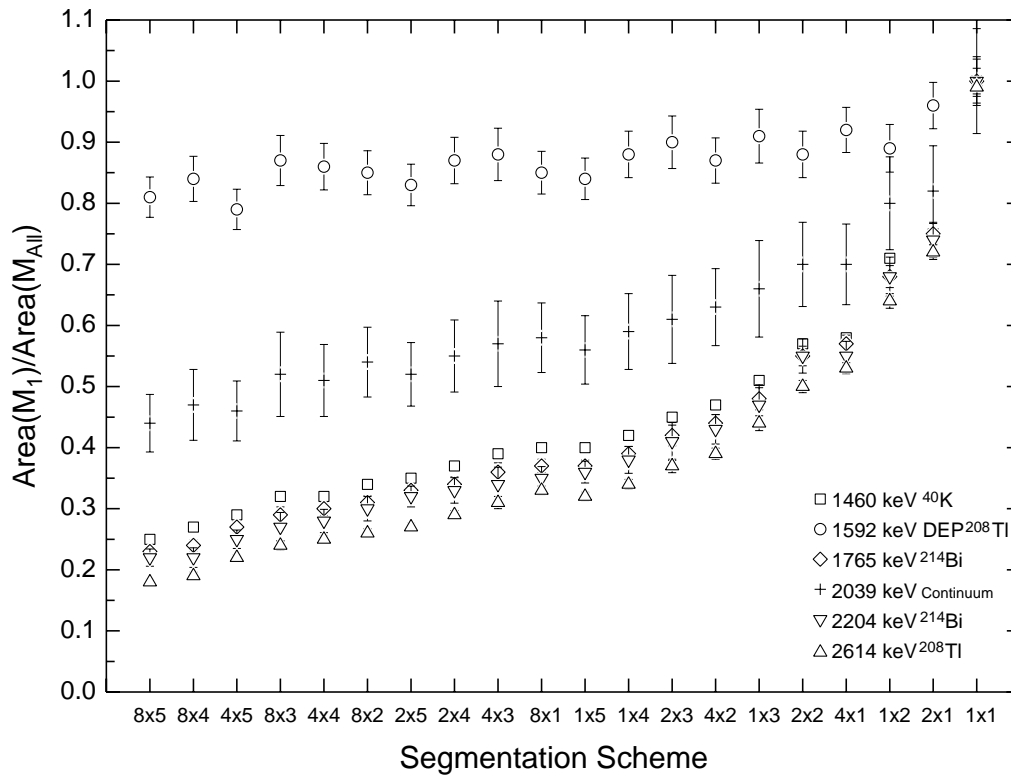
9

Fig. 5. The examined segmentation schemes ranked according to acceptance efficiency of the 1460 keV ^{40}K peak. Values for the continuum and double-escape peak are shown as well.
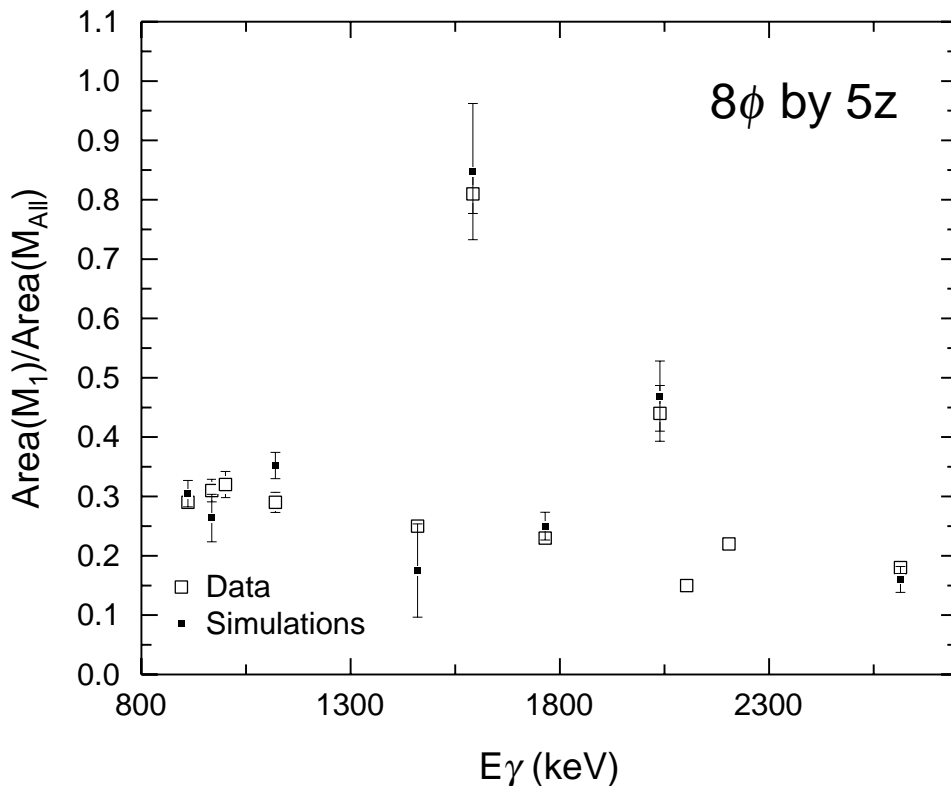
Fig. 6. A plot of both simulated and observed acceptance efficiency ratios for the 8ϕ by 5z segmentation scheme.

Table 1

<div align="center">Table of observed acceptance ratios.</div>

E_γ(keV)	8ϕby5z	8ϕby4z	8ϕby3z	8ϕby2z	8ϕby1z
911	0.29±0.01	0.31±0.02	0.36±0.02	0.40±0.02	0.46±0.02
968	0.31±0.02	0.33±0.02	0.38±0.03	0.44±0.03	0.49±0.02
1001	0.32±0.02	0.34±0.03	0.39±0.04	0.44±0.03	0.48±0.03
1120	0.29±0.02	0.30±0.02	0.37±0.03	0.38±0.02	0.43±0.02
1460	0.25±0.00	0.27±0.00	0.32±0.01	0.34±0.01	0.40±0.01
1765	0.23±0.01	0.24±0.01	0.29±0.01	0.31±0.01	0.37±0.01
2039	0.44±0.05	0.47±0.06	0.52±0.07	0.54±0.06	0.58±0.06
2103	0.15±0.01	0.16±0.02	0.20±0.02	0.23±0.02	0.28±0.02
2204	0.22±0.01	0.22±0.02	0.27±0.02	0.30±0.02	0.35±0.02
2614	0.18±0.00	0.19±0.01	0.24±0.01	0.26±0.01	0.33±0.01
1592	0.81±0.03	0.84±0.04	0.87±0.04	0.85±0.04	0.85±0.04
E_γ(keV)	4ϕby5z	4ϕby4z	4ϕby3z	4ϕby2z	4ϕby1z
911	0.34±0.01	0.37±0.02	0.44±0.02	0.53±0.02	0.64±0.02
968	0.35±0.02	0.39±0.02	0.47±0.04	0.55±0.03	0.65±0.03
1001	0.36±0.02	0.40±0.03	0.46±0.04	0.55±0.03	0.65±0.03
1120	0.32±0.02	0.36±0.02	0.45±0.03	0.50±0.03	0.61±0.03
1460	0.29±0.00	0.32±0.01	0.39±0.01	0.47±0.01	0.58±0.01
1765	0.27±0.01	0.30±0.01	0.36±0.02	0.44±0.01	0.57±0.01
2039	0.46±0.05	0.51±0.06	0.57±0.07	0.63±0.06	0.70±0.07
2103	0.20±0.02	0.22±0.02	0.27±0.03	0.36±0.03	0.49±0.03
2204	0.25±0.01	0.28±0.02	0.34±0.03	0.43±0.02	0.55±0.02
2614	0.22±0.01	0.25±0.01	0.31±0.01	0.39±0.01	0.53±0.01
1592	0.79±0.03	0.86±0.04	0.88±0.04	0.87±0.04	0.92±0.04

Table 2

<div style="text-align:center">Table of observed acceptance ratios continued.</div>

E_γ(keV)	2ϕby5z	2ϕby4z	2ϕby3z	2ϕby2z	2ϕby1z
911	0.39±0.02	0.42±0.02	0.49±0.03	0.62±0.02	0.79±0.02
968	0.41±0.02	0.43±0.03	0.52±0.04	0.64±0.03	0.79±0.03
1001	0.41±0.03	0.45±0.03	0.52±0.05	0.64±0.04	0.79±0.04
1120	0.38±0.02	0.41±0.02	0.50±0.04	0.60±0.03	0.78±0.03
1460	0.35±0.00	0.37±0.01	0.45±0.01	0.57±0.01	0.75±0.01
1765	0.33±0.01	0.34±0.01	0.42±0.02	0.55±0.02	0.75±0.02
2039	0.52±0.05	0.55±0.06	0.61±0.07	0.70±0.07	0.82±0.07
2103	0.26±0.02	0.28±0.02	0.34±0.03	0.50±0.03	0.72±0.03
2204	0.32±0.02	0.33±0.02	0.41±0.03	0.55±0.03	0.74±0.03
2614	0.27±0.01	0.29±0.01	0.37±0.01	0.50±0.01	0.72±0.01
1592	0.83±0.03	0.87±0.04	0.90±0.04	0.88±0.04	0.96±0.04
E_γ(keV)	1ϕby5z	1ϕby4z	1ϕby3z	1ϕby2z	1ϕby1z
911	0.44±0.02	0.47±0.02	0.55±0.03	0.74±0.03	1.00±0.03
968	0.45±0.02	0.48±0.03	0.58±0.04	0.75±0.04	1.00±0.04
1001	0.46±0.03	0.50±0.03	0.58±0.05	0.76±0.04	1.01±0.05
1120	0.43±0.02	0.46±0.03	0.56±0.04	0.72±0.04	0.99±0.04
1460	0.40±0.01	0.42±0.01	0.51±0.01	0.71±0.01	1.00±0.01
1765	0.37±0.01	0.39±0.01	0.48±0.02	0.68±0.02	1.00±0.02
2039	0.56±0.06	0.59±0.06	0.66±0.08	0.80±0.08	1.00±0.09
2103	0.31±0.02	0.33±0.02	0.41±0.03	0.65±0.04	1.00±0.04
2204	0.36±0.02	0.38±0.02	0.47±0.03	0.68±0.03	1.00±0.04
2614	0.32±0.01	0.34±0.01	0.44±0.01	0.64±0.01	0.99±0.01
1592	0.84±0.03	0.88±0.04	0.91±0.04	0.89±0.04	1.00±0.04

Table 3

<div align="center">

Table of simulation results.

Scheme	911(keV)	968(keV)	1120(keV)	1460(keV)
8x5	0.30±0.02	0.26±0.04	0.35±0.02	0.18±0.08
8x3	0.40±0.03	0.38±0.05	0.45±0.03	0.39±0.12
8x1	0.45±0.03	0.39±0.05	0.48±0.03	0.38±0.12
4x5	0.37±0.02	0.35±0.05	0.40±0.02	0.26±0.09
4x1	0.61±0.03	0.52±0.06	0.63±0.03	0.56±0.14
2x5	0.41±0.03	0.40±0.05	0.43±0.02	0.26±0.09
2x2	0.59±0.03	0.51±0.06	0.59±0.03	0.54±0.14
2x1	0.75±0.03	0.70±0.06	0.75±0.03	0.67±0.15
1x5	0.47±0.03	0.48±0.05	0.48±0.03	0.33±0.11
1x2	0.72±0.03	0.67±0.06	0.70±0.03	0.64±0.15
Scheme	1765(keV)	2039(keV)	2614(keV)	1592(keV)
8x5	0.25±0.02	0.47±0.06	0.16±0.02	0.85±0.11
8x3	0.34±0.03	0.49±0.06	0.28±0.03	0.60±0.10
8x1	0.37±0.03	0.56±0.06	0.33±0.03	0.90±0.12
4x5	0.34±0.03	0.55±0.06	0.21±0.02	0.87±0.12
4x1	0.57±0.04	0.67±0.07	0.48±0.04	0.93±0.12
2x5	0.40±0.03	0.57±0.07	0.25±0.03	0.89±0.12
2x2	0.56±0.04	0.59±0.07	0.49±0.04	0.64±0.10
2x1	0.76±0.04	0.75±0.07	0.70±0.05	0.95±0.12
1x5	0.45±0.03	0.64±0.07	0.28±0.03	0.92±0.12
1x2	0.67±0.04	0.68±0.07	0.62±0.04	0.70±0.10

</div>